AGU PUBLICATIONS

JGR

Journal of Geophysical Research: Solid Earth

RESEARCH ARTICLE

10.1002/2016JB013017

Where do ocean microseisms come from? A study of Love-to-Rayleigh wave ratios

C. Juretzek[1] and C. Hadziioannou[1]

[1]Department of Earth and Environmental Sciences, Ludwig-Maximilians University, Munich, Germany

Key Points:
- Seismic noise source directions and Love-to-Rayleigh wave ratios determined by means of beamforming
- Love-to-Rayleigh ratio stronger in primary than in secondary microseism
- Ratios depend strongly on direction but stay stable over seasons

Supporting Information:
- Supporting Information S1

Correspondence to:
C. Juretzek,
carina.juretzek@posteo.de

Citation:
Juretzek C., and C. Hadziioannou (2016), Where do ocean microseisms come from? A study of Love-to-Rayleigh wave ratios, *J. Geophys. Res. Solid Earth*, *121*, 6741–6756, doi:10.1002/2016JB013017.

Received 22 MAR 2016
Accepted 22 AUG 2016
Accepted article online 25 AUG 2016
Published online 27 SEP 2016

Abstract Our knowledge of the origin of Love waves in the ambient seismic noise is extremely limited. This applies in particular to constraints on source locations and source mechanisms for Love waves in the secondary microseism. Here three-component beamforming is used to distinguish between the differently polarized wave types in the primary and secondary microseismic noise fields, recorded at several arrays across Europe. We compare characteristics of Love and Rayleigh wave noise, such as source directions and frequency content, measure Love to Rayleigh wave ratios for different back azimuths, and look at the seasonal behavior of our measurements by using a full year of data in 2013. The beamforming results confirm previous observations that back azimuths for Rayleigh and Love waves in both microseismic bands mainly coincide. However, we observe differences in relative directional noise strength between both wave types for the primary microseism. At those frequencies, Love waves dominate on average, with kinetic Love-to-Rayleigh energy ratios ranging from 0.6 to 2.0. In the secondary microseism, the ratios are lower, between 0.4 and 1.2. The wave type ratio is directionally homogeneous, except for locations far from the coast. In the primary microseism, our results support the existence of different generation mechanisms. The contribution of a shear traction-type source mechanism is likely.

1. Introduction

Ocean microseisms are the continuous seismic background oscillations, which result from the interaction between the atmosphere, the ocean waves, and the solid earth. Two distinct peaks are globally observed in the microseism spectra, which differ in frequency and amplitude. The weaker single-frequency peak, centered around 14 s, is known as primary microseism peak and results from a direct interaction between ocean gravity waves with the seafloor in shallow water [*Hasselmann*, 1963]. The more energetic secondary microseism peak, which appears at about twice the primary microseism frequency (7 s), arises from pressure oscillations at the sea surface caused by interaction of opposing gravity waves [e.g., *Longuet-Higgins*, 1950; *Hasselmann*, 1963].

Already at the beginning of the twentieth century, interest in the origin of microseismic noise resulted in a significant number of studies [e.g., *Wiechert*, 1904; *Gutenberg*, 1911]. After the causal link of microseisms to ocean wave conditions had been established, the potential of monitoring, e.g., storm systems, was realized immediately and was continuously pursued by many authors [e.g., *Deacon*, 1947; *Iyer*, 1958; *Davy et al.*, 2014]. For an extensive overview of the history of microseismic noise studies, we refer to *Ebeling* [2012].

Through the use of ambient noise correlations, this microseismic noise has become an important signal source for tomography [e.g., *Shapiro and Campillo*, 2004; *Sabra et al.*, 2005] and monitoring purposes [e.g., *Sens-Schönfelder and Wegler*, 2006; *Brenguier et al.*, 2008]. Most studies that cross correlate ambient noise aim to obtain signals similar to the Green's function. In order for the equivalence to hold, one must start from the assumption that the ambient noise field is azimuthally isotropic and stable over time [e.g., *Sanchez-Sesma and Campillo*, 2006]. In practice, however, many studies use the noise in the primary and secondary ocean-generated microseismic frequency bands. Oceanic noise sources are localized and not uniformly distributed, which in some cases can lead to a bias in measurements based on ambient noise correlations [e.g., *Tsai*, 2009; *Weaver et al.*, 2009]. Therefore, a better understanding of the microseism noise field characteristics is desirable to further improve ambient noise applications.

The ocean-generated microseisms consist mostly of surface waves, as well as a smaller amount of body waves [e.g., *Toksöz and Lacoss*, 1968; *Gerstoft et al.*, 2008; *Koper et al.*, 2010; *Gualtieri et al.*, 2014]. Fundamental mode Rayleigh waves are found to dominate microseismic noise in most places. However, the excitation of different

modes is dependent on water depths [*Longuet-Higgins*, 1950; *Gualtieri et al.*, 2013] and higher mode surface waves have been observed onshore in some regions [e.g., *Brooks et al.*, 2009; *Kimman et al.*, 2012].

Nevertheless, considerable amounts of Love waves were already reported early on in microseism noise research [e.g., *Darbyshire and Iyer*, 1958; *Haubrich and McCamy*, 1969; *Rind and Donn*, 1979]. Since then, the interest in using and studying them has decreased. Hence, our knowledge about common and different origins of Love and Rayleigh waves in the microseism band is still limited. This applies in particular to constraints on source locations and generation mechanisms of Love waves, especially in the secondary microseism band.

Many recent studies concentrate on Rayleigh waves and *P* waves by focusing on the vertical component of noise. The generation mechanism of the Rayleigh and body waves in the secondary microseism band is well described by the theory of *Longuet-Higgins* [1950] and later *Hasselmann* [1963]. Their theory has since been confirmed in several studies by observations [e.g., *Kedar et al.*, 2008] and simulations [e.g., *Ardhuin et al.*, 2011; *Gualtieri et al.*, 2013].

For the secondary microseisms, no direct generation mechanism of Love waves from ocean waves is presently known. Indirect generation has been proposed, such as conversion from Rayleigh waves on the propagation path between source region and the point of observation [e.g., *Toksöz and Lacoss*, 1968]. In the case of the primary microseisms, pressure forces over inclined bathymetry during shoaling [*Hasselmann*, 1963; *Ardhuin et al.*, 2011] and shear traction [*Nishida et al.*, 2008; *Saito*, 2010; *Fukao et al.*, 2010; *Friedrich et al.*, 1998] were found to be the most plausible mechanism to generate Love wave simultaneously with Rayleigh waves in shallow water.

Already in early noise studies, the observation was made that the amount of Love wave noise found can vary considerably depending on the geographical location and direction of propagation [*Rind and Donn*, 1979]. In several studies, Love waves in the primary and secondary microseism bands were observed to propagate mainly from similar directions as Rayleigh waves [*Haubrich and McCamy*, 1969; *Nishida et al.*, 2008] and with a comparable frequency content [*Haubrich and McCamy*, 1969]. However, studying the noise wavefield around New Zealand, *Behr et al.* [2013] observed similar source directions in the secondary but different source directions in the primary microseism band.

Considering the ratio of Love to Rayleigh waves present in ambient seismic noise is one way to quantify the relative content of both surface wave types. Such a measurement simultaneously carries information about the initially generated wave type content by the source mechanism, as well as any modifications due to propagation effects. For example, *Rind and Donn* [1979] state that geologic heterogeneities along the propagation path likely affect the observed Love to Rayleigh wave ratio, by altering amplitudes of Love waves differently than those of Rayleigh waves. However, the relative amount of the wave types generated directly by a noise source will also strongly affect the observed Love to Rayleigh wave ratio.

Recent studies have aimed to quantify the Love wave content more precisely by considering the energy ratio of Love and Rayleigh waves present. They found a significant contribution of Love wave noise exceeding the Rayleigh wave content in the primary but not in the secondary microseism band [e.g., *Friedrich et al.*, 1998; *Nishida et al.*, 2008] although *Tanimoto* [2013] found comparable levels of both wave types.

Here we study the directional, seasonal, and spectral dependence of the Love wave noise content in the primary and secondary microseism bands across Europe in detail and compare these observations to Rayleigh waves. We further measure Love to Rayleigh amplitude and kinetic energy ratios and report on their dependence on direction and time. In this study, we use several arrays to be able to observe also potential local variations of these properties.

2. Data and Array Processing

In order to analyze the Rayleigh and Love wave content in the primary and secondary microseism bands, we used the available seismic data from eight seismic station sets distributed around Europe during the year 2013. The array locations and geometries are displayed in Figure 1. Data from the permanent three-component arrays Gräfenberg (GRF) and Norsar (NOA), as well as from four station sets of suitable geometries from the European network (CH, IT, NICE, and THU), were retrieved from public data centers. Additionally, two nonpublic arrays were used, the Donegal array (IRE, from the Dublin Institute for Advanced Studies, DIAS) and the Morocco Münster array (MM, described by *Spieker et al.* [2014]). Due to the array dimensions, the IRE

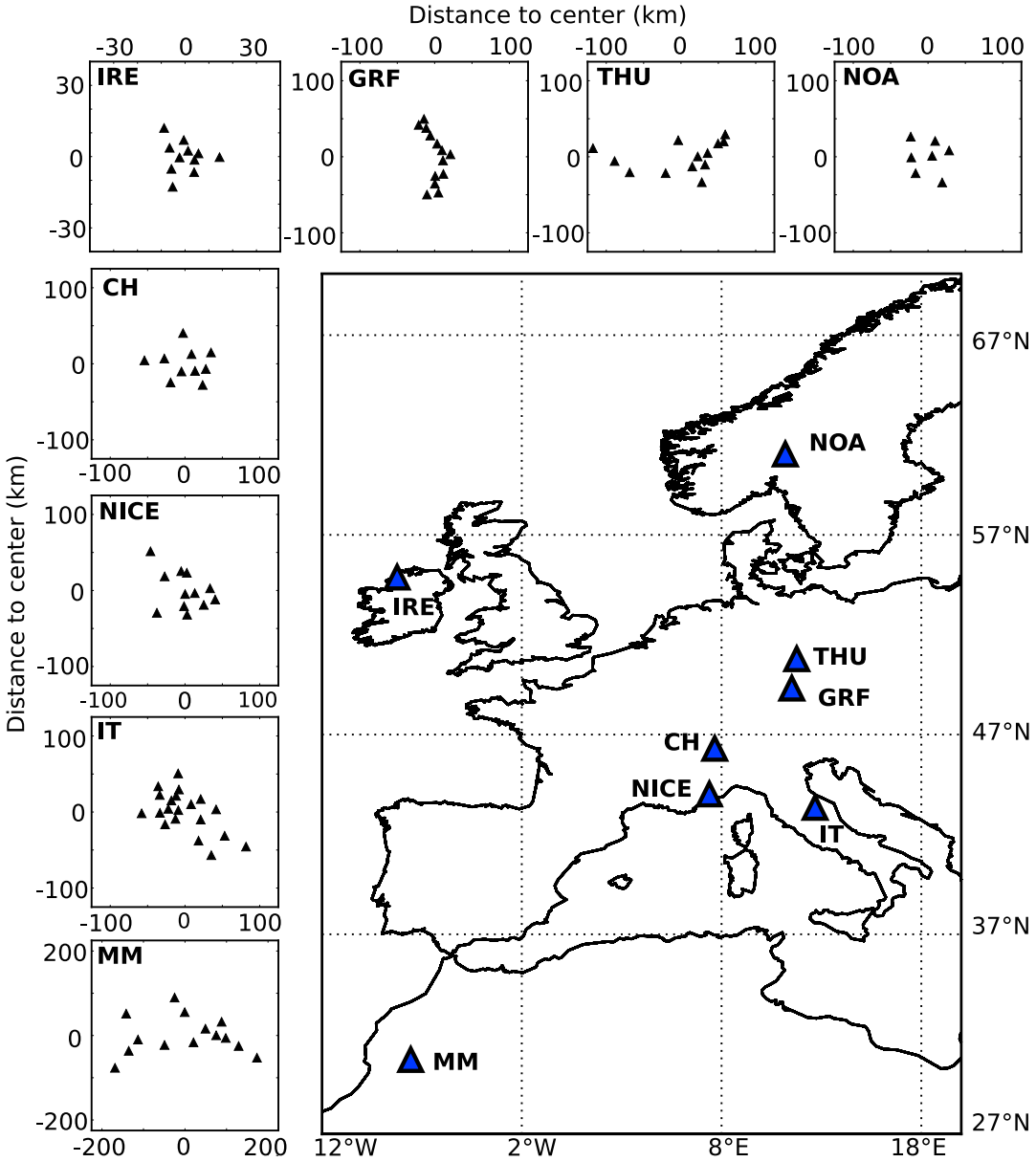

Figure 1. Center locations (triangles in map) and geometries of arrays used in this study.

network is mainly suitable for the shorter-period range of this study. For the MM network, data in 2013 were available from January to the beginning of April. The dimensions of this array suit the longer-period range better.

For the analysis of microseisms in 2013, the data were corrected for instrument response, band-pass filtered between 0.25 Hz and 0.04 Hz and downsampled to 1 Hz. The three-component velocity seismograms were split into nonoverlapping time segments of 1024 s using a Tukey window. The influence of earthquakes was reduced by the applications of a Short Time Average over Long Time Average (STA/LTA) filter, discarding time segments for which the vertical component data had a higher average power than twice the day average. For these processing steps we made use of the ObsPy toolbox [*Beyreuther et al.*, 2010]. We use a three-component beamforming method [*Esmersoy et al.*, 1985] in the frequency domain to distinguish differently polarized waves and to obtain estimates of the beam power, back azimuth, and slowness of incoming coherent signals in the ambient noise field. The three-component formulation was described in detail by *Riahi et al.* [2013] and is analogous to single-component beamforming. The beamforming approach is briefly summarized here.

For a N station array, the three-component, classical plane wave frequency wave number beam power estimate as a function of polarization ρ, frequency f, back azimuth θ, and slowness u can be written as

$$P\left(f,\theta,u,\rho\right)=\frac{1}{N^2}\mathbf{w}_{3N}^{*}\left(f,\theta,u,\rho\right)\mathbf{R}_{3N}(f)\mathbf{w}_{3N}\left(f,\theta,u,\rho\right), \tag{1}$$

where $\mathbf{R}_{3N}(f)$ represents the temporally averaged cross-covariance matrix of the three-component data Fourier transforms; here $*$ indicates the conjugate transpose operator. The weight vector is given by

$$\mathbf{w}_{3N}=\left[p_x e_1,\ldots,p_x e_N;p_y e_1,\ldots,p_y e_N;p_z e_1,\ldots,p_z e_N\right]^T. \tag{2}$$

It contains the phase delays for each sensor due to wave propagation in the N component vector $\mathbf{e}_N$ and the amplitude factors and phase delays for each component due to the polarization in the three-component vector $\mathbf{p}_{xyz}$. The cross-covariance matrix is temporally averaged over four consecutive time windows, giving approximately hourly beam power estimates. Fundamental mode Rayleigh waves are assumed to be retrograde polarized, with varying ellipticity angle. Love waves are assumed to be purely transversally polarized. For both Rayleigh- and Love-type polarizations, we search through a parameter space of slowness in 0.02 s/km steps and back azimuth in 2° steps. For Rayleigh waves we additionally test for the ellipticity angle in steps of 10°. The beamformer response represents the beam power estimate as $P\left(f,\theta,u,\rho_L\right)$ of the transversal component T^2 for Love waves and $P\left(f,\theta,u,\rho_R\right)$ of the vertical and radial components $R_z^2+R_r^2$ for Rayleigh waves.

3. Method Performance and Resolution

Since the availability of individual stations varies throughout the measurement period (i.e., data gaps for certain stations), the array geometry changes accordingly over time. The array transfer function is dependent on the array geometry; hence, it fluctuates with station number. Further, the array transfer function indicates the resolution capability of an array and potential risk of wrongly determined signal parameters due to side lobes. To maintain both a stable array transfer function and a good temporal observation coverage, we defined a threshold number for each array, above which the beamforming result is included. A table, detailing the threshold, the maximum, and the average station number per array, is provided as supporting information S1.

For each array we analyzed the availability of individual stations throughout the year. The operational duration for each station configuration above the threshold number was determined. Figure 2a shows the array transfer functions for an incoming plane wave with zero slowness at a period of 8 s, using the array configurations with maximum operational duration in the analysis above, i.e., configurations which were most frequently available.

In the usual case for microseisms, the presence of multiple signals, the propagation parameters, and beam power of the signals were shown to be practically retrievable if the number of stations in an array is large enough and if the signal propagation parameters are not too closely related (for more details, see, e.g., *Poggi and Fäh* [2010]). Due to the different array geometries, the beamformer capability to separate coexisting signals varies with the arrays used here. We use a synthetic data set to test the capability of the three-component beamforming algorithm to distinguish between Love and Rayleigh waves for the different arrays used here. Moreover, we investigate to what extent the relative signal strength for each wave type is recovered in the presence of additive unpolarized noise. The synthetic three-component data consist of the superposition of a retrograde polarized Rayleigh wave, a transversally polarized Love wave, and unpolarized additive noise in the time domain. We use single-period signals and set the total data length to 3 times the synthetic signal period considered (e.g., at a signal period of 8 s). The surface wave signals are plane waves of uniform amplitude. The phases between the wave types are uncorrelated. Two unpolarized noise signals with random values for slowness, direction, and initial phase from a Gaussian distribution and a total amplitude of either 0.5 or 1.0 were equally distributed over the three components. For each test, 60 realizations of the synthetic data set were calculated.

Figure 2b shows the performance test for the array geometries of GRF and IRE at a period of 8 s. For each wave type, the mean of the 60 individual beamformer outputs is plotted, along with the distributions of the Love to Rayleigh wave ratios. We consider two cases: when the Rayleigh and Love waves are coming from

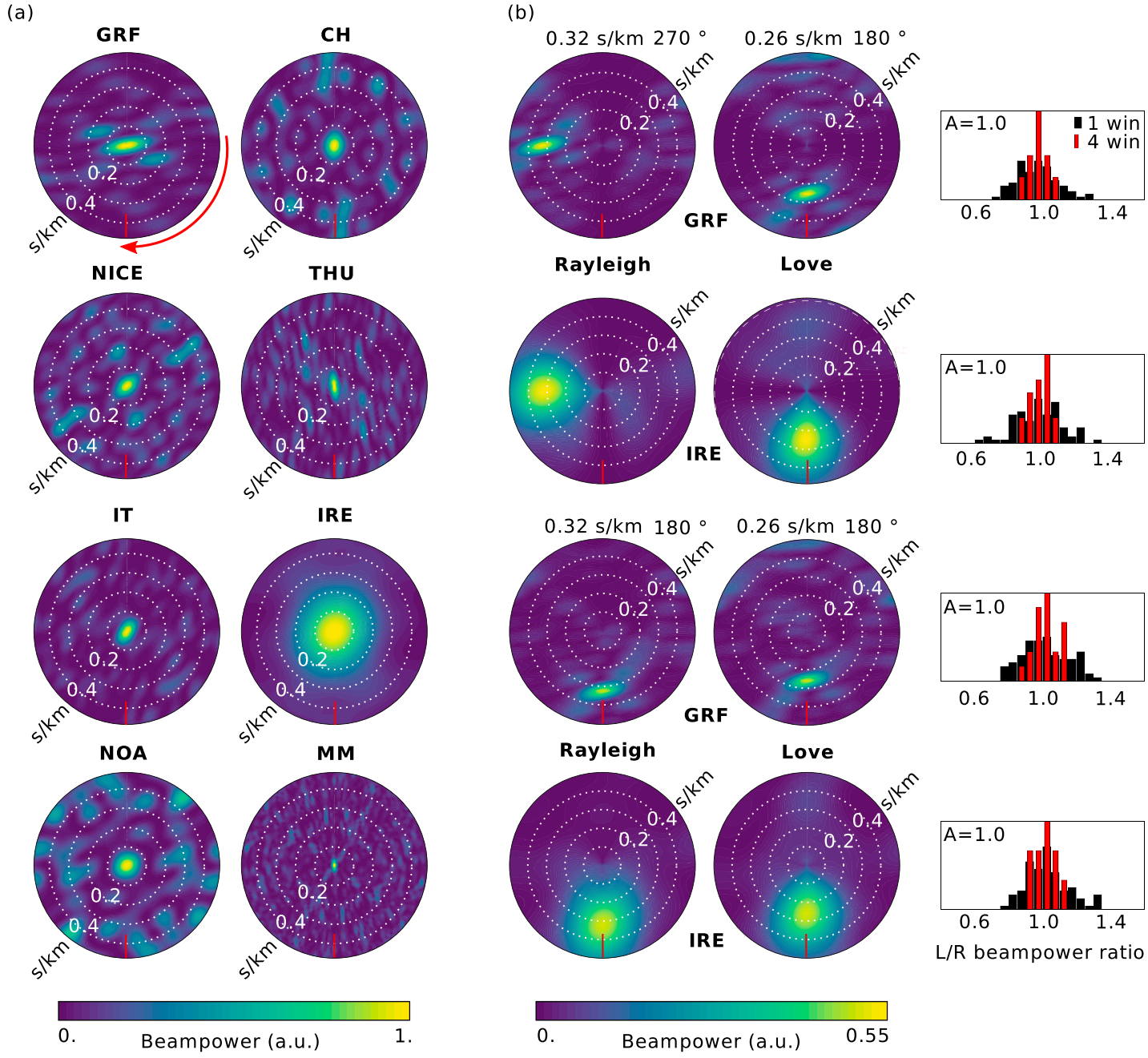

Figure 2. (a) Slowness versus back azimuth (clockwise) representations of the response functions of the arrays used at a period of 8 s. (b) Beamformer performance test for the array geometry of GRF and IRE with a synthetic data set at 0.125 Hz. Data consist of one Love and one Rayleigh wave polarized plane wave of uniform amplitude from (top) different source directions and (bottom) same source direction and two additive uncorrelated noise signals with a total amplitude of $A = 1.0$. The polar graphs show the average beam power output for each wave type. Labels above indicate back azimuth and slowness of synthetic signals. The histograms show the spread of the wave type beam power ratio for single time windows (black thick bars) and for averaging over four consecutive time windows (red thin bars). A back azimuth of 180° is marked by a red dash.

the same direction and when the wave types' angles of approach are perpendicular to each other. For both additive noise level amplitudes, the correct back azimuth and slowness values are obtained. The wave type ratios are distributed around the correct ratio of 1.0 but may be spread out considerably for the higher noise level case. Averaging the cross-covariance matrix over four time windows before beamforming, as applied in our data analysis, decreases the spread considerably. Since we are interested in average properties here, the three-component beamforming analysis should recover a satisfactory approximation of the average wave

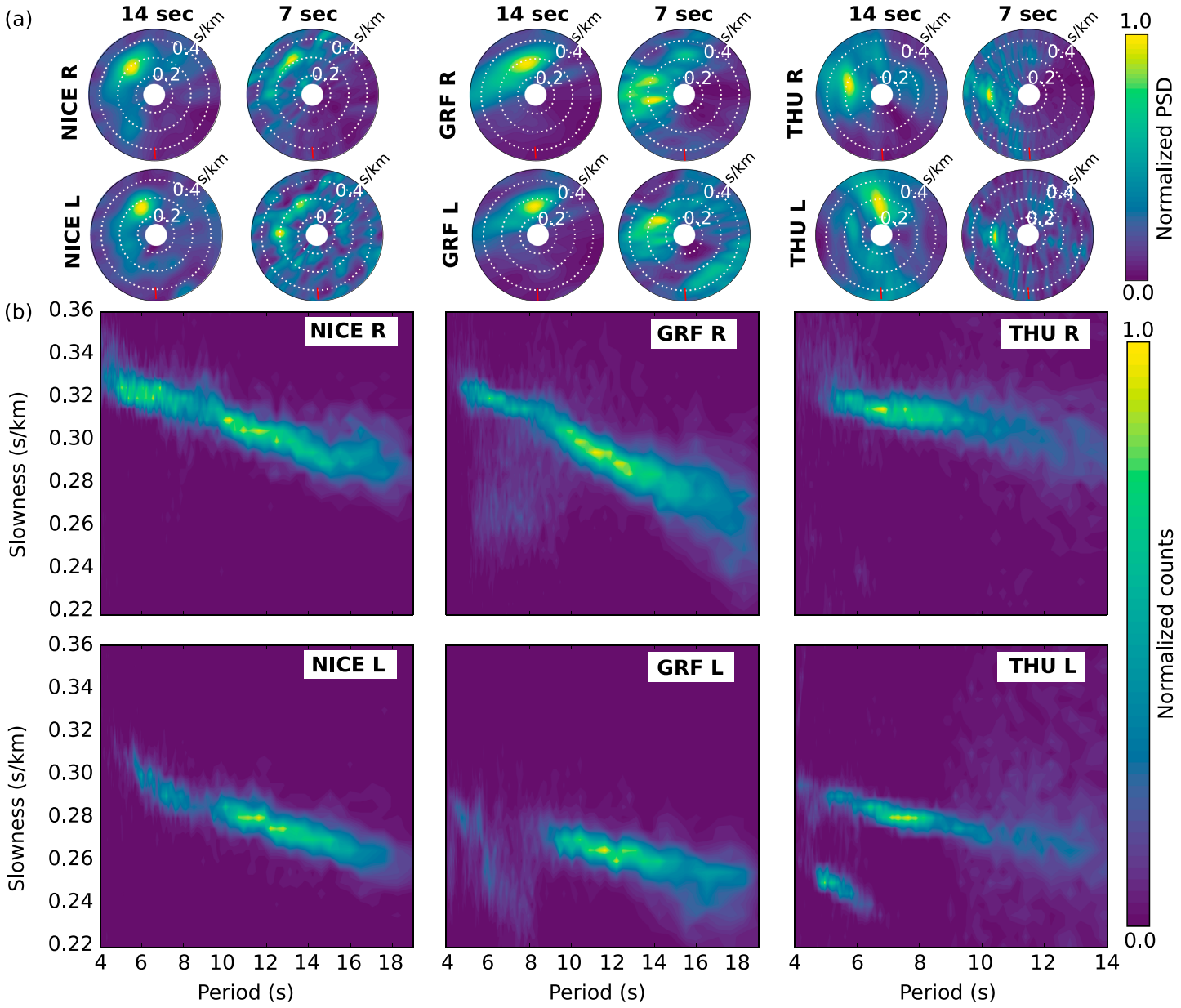

Figure 3. (a) Slowness versus back azimuth representations of beamforming results for Rayleigh and Love waves at NICE, GRF, and THU. (b) Examples of frequency-dependent slowness at the corresponding arrays.

type ratio, when considering only the strongest signals observed. We further tested the wave type ratio recovery in the synthetic test using the minimal number of station configurations. Also in this case, the expected ratio could still be retrieved on average (cf. Figure S2 in the supporting information).

In order to minimize the number of misdetections, we discard beamforming results that do not match the expected surface wave phase velocity range. Therefore, we determine average local dispersion curves for Love and Rayleigh waves at each array by performing beamforming for a finer slowness spacing ($0.005\ \frac{s}{km}$) over a few months. Figure 3a shows examples of self-normalized yearly median beam power spectral density over back azimuth and slowness, determined at periods of 7 and 14 s. For the three arrays shown here, the directions of approach of Love waves correspond to distinct back azimuths which are often similar to those of Rayleigh waves. However, the relative wave type strength varies for different source directions, which is especially obvious for the THU array at a period of 14 s and the GRF array at a period of 7 s. For each time window and each frequency, the slowness corresponding to the maximum of the beamformer power is selected. The

slowness picks, summed over the course of up to 3 months, are normalized, and three examples are plotted in Figure 3b. We aim to restrict our analysis to fundamental mode surface waves. However, the dispersion plots for the GRF array and especially the Love wave result for the THU array indicate a frequent occurrence of signals of higher phase velocity than the emerging fundamental mode branch. Those were hence muted for the purpose of our analysis. The dispersion curves are then retrieved as a smoothed version of the mean slowness at each frequency $\overline{u}(f)$. We also determine the standard deviation $\sigma_u(f)$ of the slowness distribution at each frequency. In the remainder of this analysis, we reject beamformer results outside the slowness range $\overline{u}(f) \pm \sigma_u(f)$ to improve the separation between random and polarized noise and to confine our analysis to fundamental mode observations.

4. Signal Source Directionality

We use the outlined beamforming method to decompose the ambient noise field into Love and Rayleigh wave polarized signals. We are interested in spatial and directional characteristics of the surface wave noise composition. For each time segment and frequency bin we determine the back azimuth corresponding to the maximum beam power of Love and Rayleigh wave polarized signals, respectively, which fulfill the slowness range criteria. A number count histogram of the entire year results is collected with azimuthal bins of 6°.

Figure 4 shows the radial histogram plot of the dominant surface wave type observations over back azimuth for all array sites, averaged over the primary (13–15 s) (a) and the secondary (5–7 s) (b) microseism peaks. The radial axis shows normalized counts per direction within back azimuth bins of 6°.

The primary microseism Rayleigh wave noise in Europe most frequently originates from northern and northwestern back azimuths, pointing toward the coast of Norway and the British Isles. Both of these regions are well known to be the origin of some of the stronger microseismic signals in Europe [e.g., *Friedrich et al.*, 1998]. This correlates well with average ocean wave parameters in 2013. As shown in the inset of Figure 4a, the western European coasts are exposed to high average ocean wave heights. In comparison to Rayleigh waves, dominant Love wave noise contributions from the north are even more frequent. Toward the southern array sites, contributions from the Atlantic coast and British Isles region more equally dominate for both wave types.

At the NOA array, which is located nearby the Norwegian source regions, preferred source directions of Love and Rayleigh waves differ clearly. The North African array MM shows a comparable pronounced difference between both wave types. Rayleigh waves are mainly observed from the coast directly to the northwest, while Love waves originate from more northern and southwestern back azimuths. Generally, the directional spread in the Love wave back azimuths is smaller than for Rayleigh waves.

In the secondary microseism band, Rayleigh wave observations outnumber the occurrence of coherent Love wave observations. The most frequent dominant noise contribution for Rayleigh waves corresponds to back azimuths pointing toward the North Atlantic, the British Isles region, and offshore Norway. This is in agreement with observations by, e.g., *Friedrich et al.* [1998], *Essen et al.* [2003], *Kimman et al.* [2012], and *Kedar et al.* [2008], who find strong microseismic Rayleigh waves from the same regions. Furthermore, these observations correlate with the locations of high average wave-wave interaction induced secondary surface pressure in 2013 (inset of Figure 4b).

The directions of approach of dominant Love waves correspond to distinct back azimuths, which are similar to those of Rayleigh waves. However, at central European sites the relative occurrence frequency for particular source directions differs between Love and Rayleigh waves. At GRF, THU, CH, and NICE, the most frequent dominant Love wave contributions are commonly observed from northwestern back azimuths, in the direction of the British Isles and the North Atlantic, while contributions from the remaining back azimuths are weaker on average. The occurrence of Love waves seems to always be accompanied by Rayleigh waves from similar directions. On the other hand, back azimuths exist from which Rayleigh wave occurrence dominates, without clear Love waves from the same direction. This means that the observation of Love wave signals which unambiguously meet our detection criteria is less frequent; i.e., if present, they may be unresolvable for our beamformer due to background noise. For Love waves, the range of source directions is generally broader compared to Rayleigh waves. Since average ocean wave periods in the Mediterranean Sea are relatively short, in addition to the secondary microseism, we expect to also observe microseisms generated by primary source mechanisms for periods of 5–8 s at, e.g., the Italian array (IT).

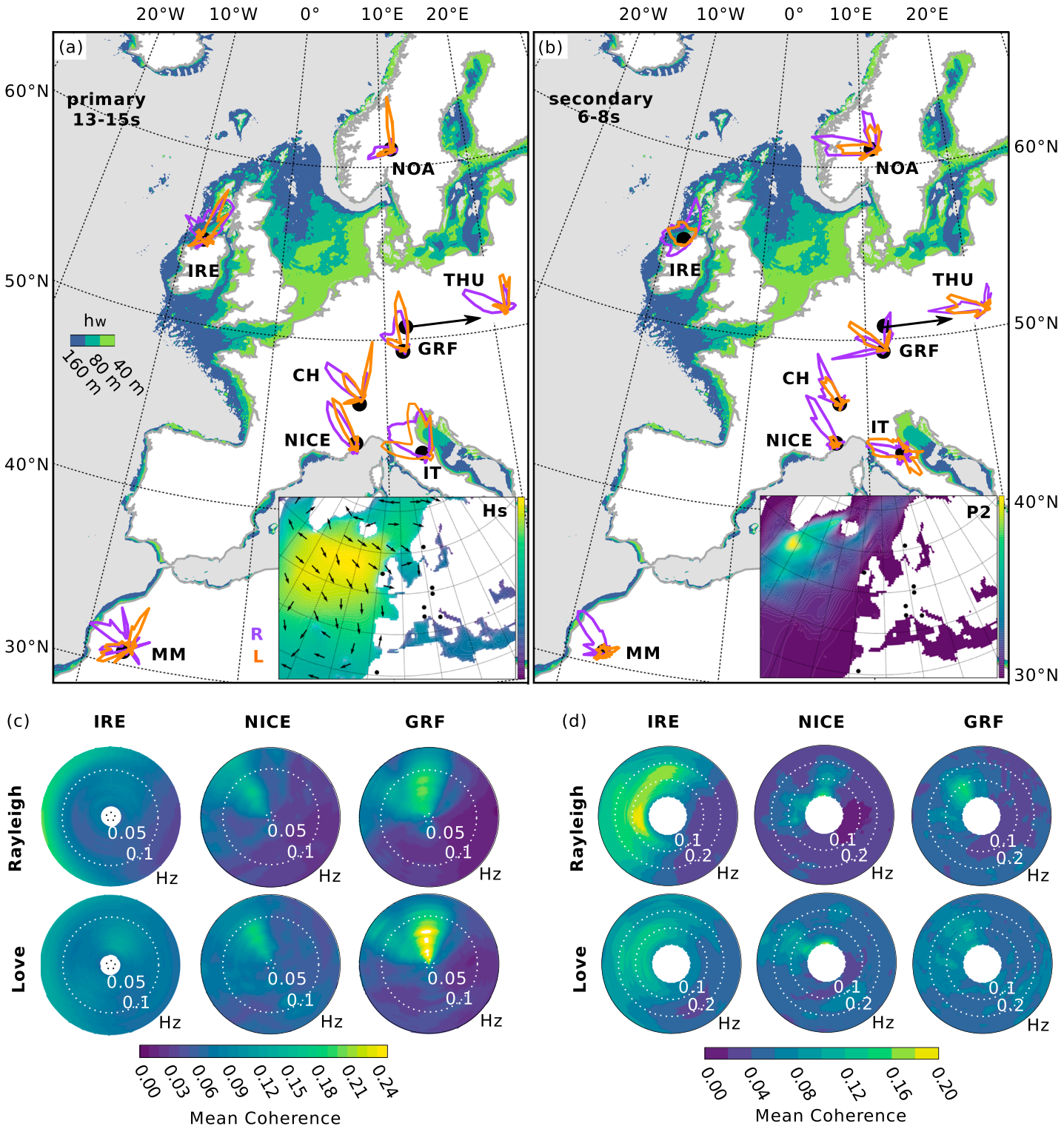

Figure 4. Yearly wave type source direction counts in 2013 at different array sites around the (a) primary (13–15 s) and (b) secondary (6–8 s) microseism peaks (per array, same scale for each wave type). For the period range considered, intermediate water depths (h_w) are indicated by colored contour levels in the map. Yearly averaged wave type coherence over back azimuth and frequency for (c) the primary and (d) the secondary microseism range in 2013. Figure 4a inset shows average significant wave height and most frequent mean ocean wave directions in 2013. The color scale ranges from 0 to 4 m. Figure 4b inset shows average wave-wave interaction induced surface pressure in 2013 as provided by *Ardhuin et al.* [2011]. The color scale ranges from 0 to 10^8 Pa^2 m^2 s.

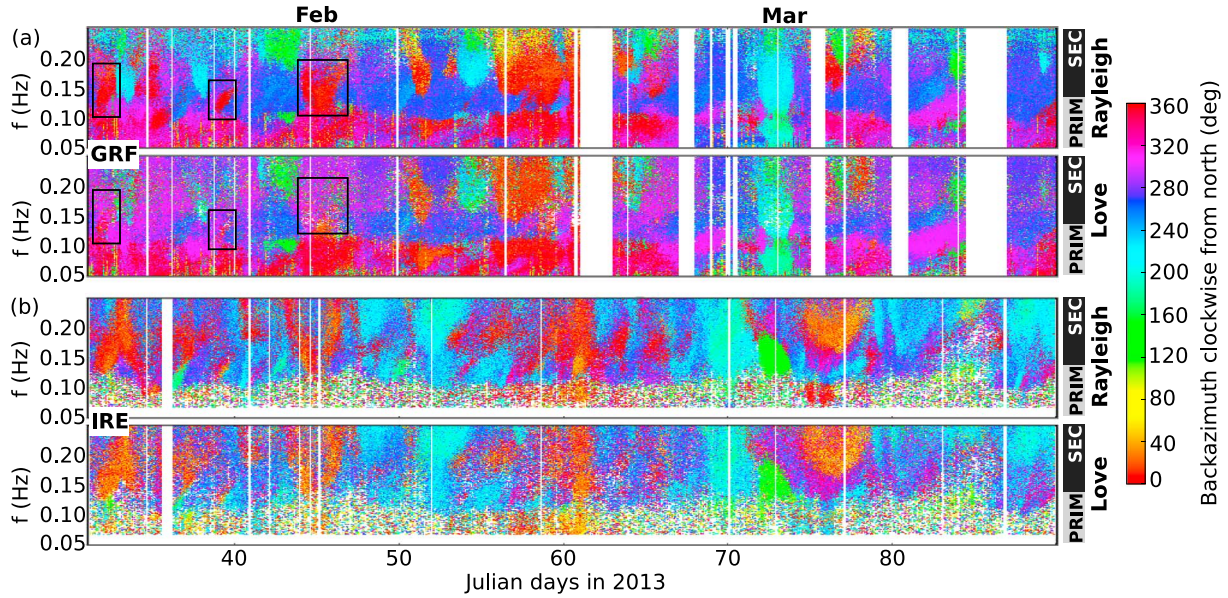

Figure 5. Frequency-dependent signal back azimuths (color scale) of both wave types from February to March 2013, comparison of measurements at the arrays (a) GRF and (b) IRE. White areas correspond to periods of missing or rejected data. Black rectangles indicate the observation discussed in section 4.

For a comparison between source directions of both wave types across the whole frequency range of interest we look at the temporally averaged wave type coherence within the expected surface wave velocity range in dependence on back azimuth and frequency as depicted for the arrays IRE, GRF, and NICE in Figures 4c and 4d. Here the coherence for Love waves is given by the ratio between the beam power and the horizontal component power ($X^2 + Y^2$) averaged over all array stations, respectively, for Rayleigh waves as ratio between beam power and three-component power ($X^2 + Y^2 + Z^2$) averaged over all array stations. In both microseism bands the source directions of persistent wave type signals agree well across the whole frequency range analyzed.

A more detailed comparison of the time-dependent behavior of Love and Rayleigh waves is given in Figure 5, which shows the frequency-dependent dominant signal back azimuths (color scale) of each wave type over a period of 2 months, from February to March 2013. Shown are the observations for the arrays in Ireland (IRE) and in central Europe (GRF). White gaps indicate periods of rejected or missing data. When visually comparing the two plots in Figure 5a, we find a high similarity of temporal and spectral variations between Rayleigh and Love wave source directions in the primary microseism range at GRF (approximately 8–20 s). Frequently, both wave types are jointly observed from northern (red colors) and western to northwestern back azimuths (blue and pink colors).

In the secondary microseism range (below approximately 8 s) dominant signal back azimuths for both wave types at IRE show strong similarities (cf. Figure 5b). At the GRF array, which is located farther away from strong secondary noise sources, differences in dominant source directions are visible. For instance, during coherent Rayleigh wave noise observations from northern back azimuths, the Love wave noise is rarely dominated by signals from corresponding directions (areas in plot indicated by black rectangles in Figure 5a).

5. Wave Type Ratio Directionality

The differences in source directionality between dominant signals of both wave types indicate that the Love to Rayleigh wave ratio must also be directionally heterogeneous. In order to investigate the directional dependence of the Love to Rayleigh wave ratio in detail, we determine beam power ratios for specific source directions. We select directions for which the strongest signal of both wave types is observed simultaneously (time segment of approximately 1 h) from a common source back azimuth range of 20°. For signals meeting those criteria, we calculate the wave type ratio using the maximum beam power of both wave types and allocate it to the mean back azimuth of both. Possible propagation path deviations and travel time differences from the source are assumed to be accounted for by the chosen time and back azimuth range.

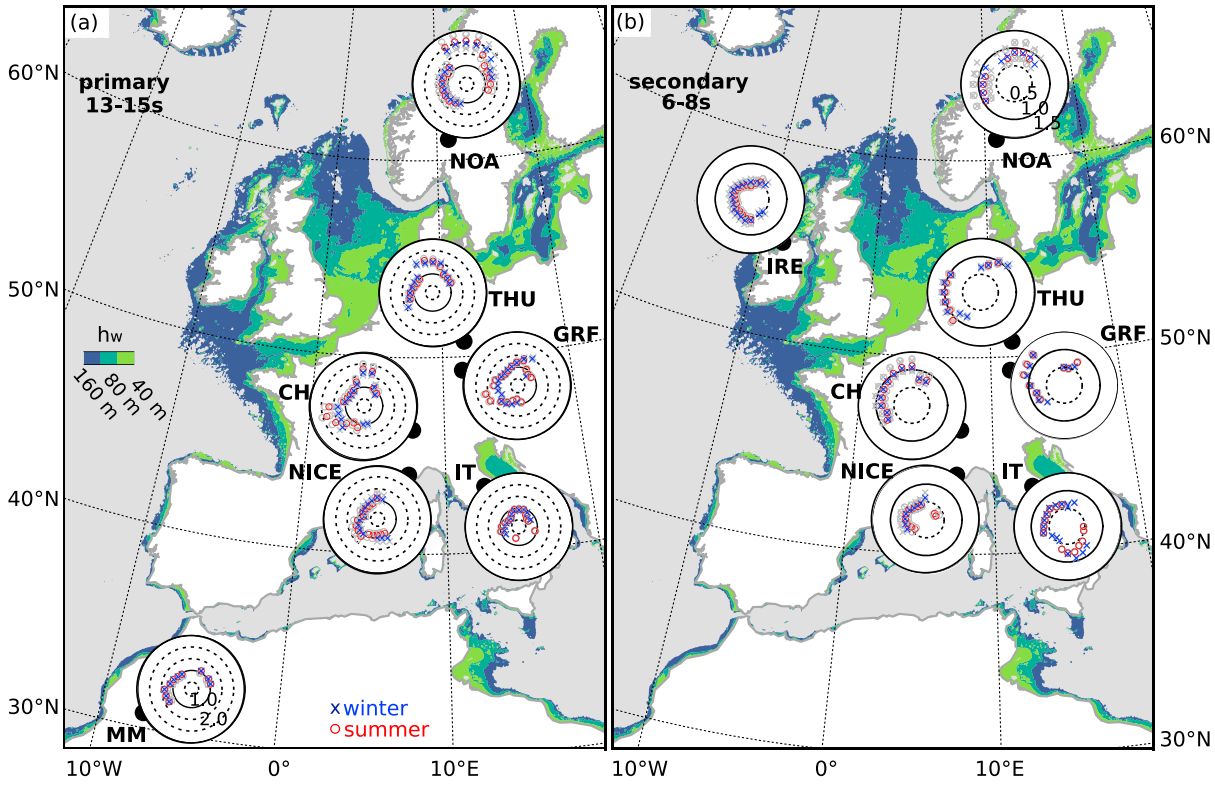

Figure 6. Direction-dependent average summer (April–September, circles) and winter (October–March, crosses) Love/Rayleigh wave kinetic energy density ratios for (a) the primary (13–15 s) and (b) the secondary (6–8 s) microseism peak. The gray symbols show ratio uncertainty ranges corresponding to velocity structure deviations according to the dispersion curve standard deviation range.

Since the beam power ratio corresponds to a measure of surface amplitudes, the ratio determined in this way is affected by the local subsurface structure. Since the subsurface structure varies from array to array, a direct comparison between beam power ratios at the different sites is inaccurate. In a second step, we therefore estimate the ratio between Love wave and Rayleigh wave kinetic energy densities (E_L and E_R, respectively) [e.g., *Harkrider and Anderson*, 1966] under consideration of the local structure at the array sites.

Here at each frequency the kinetic energy density ratio is given by

$$E_L/E_R = \int_0^{z'} \rho T(z)^2 \mathrm{d}z \left(\int_0^{z'} \rho \left(R_z(z)^2 + R_r(z)^2 \right) \mathrm{d}z \right)^{-1}. \quad (3)$$

The eigenfunctions for the local velocity structure are denoted by $T(z)$ for Love waves and $R_z(z)$ and $R_r(z)$ for vertical and radial Rayleigh wave displacements, respectively, and were calculated with the software package by *Herrmann* [2013]. They are scaled such that their ratio at the surface corresponds to the measured wave type ratio.

A comparison of our dispersion curve measurements and theoretical dispersion curves from the reference velocity model CRUST1.0 [*Laske et al.*, 2013] at grid points near our array centers shows deviations that are not negligible especially for periods below 10 s. We retain the *P* wave velocity profile, the density profile, and the layer geometry from the CRUST1.0 model. For Rayleigh and Love waves separately, we use our corresponding fundamental mode dispersion curve measurements to invert for the anisotropic *S* wave velocity in the shallow crust using *geopsy* [*Wathelet*, 2008]. Since the kinetic energy density ratios are sensitive to variations in the assumed velocity structure, we analyze the changes in the velocity profiles due to changes in the dispersion curve measurements. Therefore, we also determined the *S* wave velocity profiles at both uncertainty limits of the considered dispersion curve slowness range $\overline{u} \pm \sigma_u$.

Figure 6 shows the resulting direction-dependent kinetic energy density ratios and their uncertainty ranges in gray, smoothed with a moving back azimuth window of 30° for the primary (13–15 s) (a) and secondary (6–8 s) (b) microseism peaks.

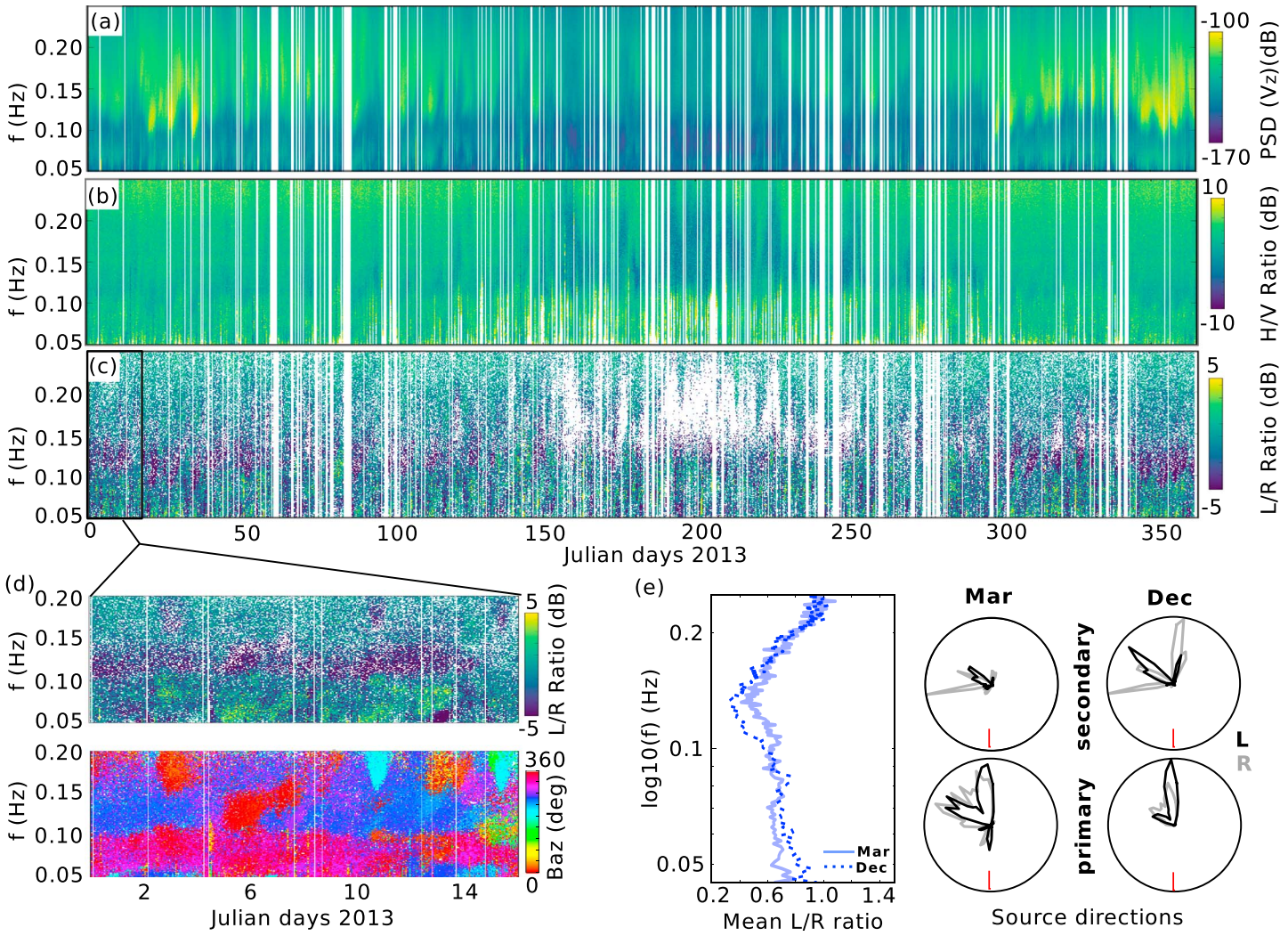

Figure 7. Seasonal variation at GRF of the (a) array averaged vertical component power spectral density, (b) array averaged horizontal/vertical components power spectral density ratio, and (c) Love/Rayleigh wave beam power spectral density ratio. (d) Short-term comparison of Love/Rayleigh wave beam power spectral density ratio (top) and corresponding source directions of Rayleigh waves (bottom). (e) Directionally averaged beam power spectral density ratio variation for different months, corresponding to different source directions being active (polar plots, right-hand panel).

In the primary microseism band, most arrays show a pronounced directional variation of the wave type ratio. For the central European arrays (CH, GRF, IT, NICE, and THU), the largest ratios are commonly found for northern and southwestern back azimuths. At NOA, the azimuthal heterogeneity is most prominent. In almost all cases, Love waves dominate with ratios larger than 1 on average.

Secondary microseism ratios show less directional dependence at most array sites. However, at central European arrays (THU, GRF, and CH) the ratio peaks toward northwestern back azimuths, corresponding to the directions of highest noise occurrence in Figure 4b. Kinetic energy ratios in the secondary microseism vary with array site and direction between about 0.4 and 1.2. At both microseism peaks, the wave type ratio direction pattern remains considerably stable between the summer and winter periods.

6. Seasonality

Figure 7a shows a full year spectrogram of the vertical component seismograms averaged over the array GRF. The higher amplitudes in the secondary and lower amplitudes in the primary microseism are apparent. Moreover, the well-known seasonal variations in noise amplitudes in both microseism bands are clearly present [*Stutzmann et al.*, 2009]. In comparison, Figures 7b and 7c show the spectrograms of the ratio between array averaged horizontal to vertical component seismograms (H/V) and of the ratio between maximum Love

to Rayleigh wave beam power (L/R) at GRF, respectively. White lines in Figures 7a–7c mark discarded periods either due to the minimum number of station criterion as explained in section 3 or due to the STA/LTA rejection criterion as explained in section 2. In Figure 7c, white gaps further correspond to frequencies at which beamforming results were rejected due to the slowness range criterion as given in section 3.

On a seasonal scale, we observe a decrease of the H/V ratio (Figure 7b, darker colors) in the secondary microseism band during Northern Hemisphere summer months. This decrease in H/V ratio does most likely not correspond to a seasonal variation in ratio of coherent Love and Rayleigh wave noise as we do not observe a significant simultaneous alteration in Figure 7c. By analyzing the *P* wave beamform results (see Figure S3 provided in the supporting information), we notice an increase in *P* wave noise levels arriving from southern back azimuths during summer, contributing to the vertical power spectrum. Such *P* waves could be likely attributed to strong distant storms, as observed by, e.g., *Gerstoft et al.* [2008] and *Zhang et al.* [2010]. The observation would also be in agreement with the expected dominance of *P* wave noise over Rayleigh wave noise with increasing distance due to lower attenuation at secondary microseism frequencies, as observed by *Landès et al.* [2010] and expected from modeling results [*Ardhuin and Herbers*, 2013]. Therefore, we attribute the variation in Figure 7b to the relative increase in *P* wave noise compared to Rayleigh wave noise. However, *Tanimoto et al.* [2006] also showed the possible relation between seasonal H/V ratio variations and differences in the modal content connected to seasonally changing source region depths. As our analysis is limited to coherent signal observations of the fundamental mode surface waves, a potential relative variation in modal content or incoherent (weak) signal ratio cannot be resolved.

As the zoom into the wave type ratio shows (Figure 7d), a variation in ratio on short time scales (hours/days) is clearly visible and correlates well with noise arrivals from varying back azimuths. When considering directionally averaged wave type ratios of simultaneously observed wave types, as in Figure 7e for 1 month periods in spring and autumn, we observe a variation in wave type ratio with time. We also plot the corresponding source direction occurrence of both wave types during the same time periods. We notice clear temporal variations in relative contributions from different source areas in both microseism bands. As we observed a temporally stable azimuthal wave type ratio pattern in Figure 6, the directionally averaged wave type ratio variations can be attributed to a varying contribution of source areas with time.

The most pronounced spectral attribute in Figures 7c and 7e is the distinct step in ratio between the primary to secondary microseism frequencies around 0.1 Hz. This was also observed by others [*Nishida et al.*, 2008; *Friedrich et al.*, 1998] and clearly hints at different capabilities of the source mechanisms to generate Love waves in the primary and secondary microseism bands.

7. Discussion

7.1. Primary Microseisms

The analysis of the average properties of surface waves in the microseismic noise field once more showed the different proportions of Love waves in the primary and secondary microseism bands. For the primary microseism band, the main findings can be summarized as follows.

1. Love waves were found to dominate the coherent noise field on average.
2. Further, common noise source directions were observed on average for both wave types, but with clearly different relative occurrence frequency (Figure 4a).
3. The difference in directivity of the wave type strength is also supported by the observed directional dependence of Love to Rayleigh wave ratios (Figure 6a).
4. The directional pattern of the wave type ratio exhibited low seasonal variations.

While local crustal heterogeneity and anisotropy could also cause directional ratio variations, the stability of the directional pattern across Europe and the magnitude of the ratio variability makes a dominance of these contributions unlikely. Therefore, the cause of the directional ratio pattern is likely related to the source mechanism.

The primary microseism is commonly believed to be generated in shallow water at water depths (h_w) of much less than the ocean wave wavelength (λ_w), e.g., $2\pi h_w/\lambda_w \ll 1$ [*Hasselmann*, 1963]. At the primary peak, this would mainly correspond to the region within the shallowest depth contour in Figures 4 and 6.

Two source mechanism types are proposed to explain horizontal component seismic noise generation. Ocean gravity waves in shallow water could generate shear tractions either (1) directly, due to friction between the

ocean wave particle motion and the seafloor [*Friedrich et al.*, 1998] or as the water propagates over seafloor topography as described in *Saito* [2010] and *Fukao et al.* [2010], or (2) indirectly, as the water propagates over inclined topography, pressure sources generated during shoaling also lead to a horizontal force component proportional to the seafloor slope [e.g., *Hasselmann*, 1963; *Ardhuin and Herbers*, 2013]. This mechanism was shown to be capable of describing observed noise levels of the vertical hum [*Ardhuin et al.*, 2015].

Individually occurring, these source mechanisms would generate both Rayleigh and Love waves at approximately the same location. We would therefore expect to observe both wave types from similar directions in general. However, the relative amount of Love or Rayleigh waves generated would be different for each mechanism: the first type would be expected to generate more Love waves than the second. This means that the observed wave type ratio could depend on source mechanism. Moreover, the radiation pattern of each wave type will be different: given that water waves propagating perpendicularly toward the coast, Rayleigh waves radiate either symmetrically or most strongly toward onshore, while Love waves radiate alongshore [e.g., *Friedrich et al.*, 1998; *Ardhuin et al.*, 2015]. Therefore, the wave type ratio observed at a certain position also depends on the respective radiation pattern, and an observation of high-amplitude Love waves noise is more dependent on an appropriate array position.

In general, at all array locations, we observe high portions of Love waves, with similar average source directions as the Rayleigh waves. This strongly supports the hypothesis of a significant contribution by excitation mechanisms that primarily induce a horizontal force, e.g., a shear traction source type. Mainly coinciding source directions and a dominance of Love waves were also observed for Japan by *Nishida et al.* [2008], who suggested a shear traction as the common source of primary microseisms.

Friedrich et al. [1998] stated that the primary microseisms are likely generated by multiple source mechanisms simultaneously, which dominate in slightly different areas. Hence, source directions can be expected to agree, in general, but deviate in detail. This is supported by our observations at several arrays, as well as by *Friedrich et al.* [1998], where the azimuthal range of incident noise directions appeared to be broader for Rayleigh waves than for Love waves (Figure 4a). In a different study, *Matsuzawa et al.* [2012] observed moderately differing source directions for both wave types when tracking a strong storm near the Norwegian coast. The authors conclude that the wave types are generated by different source mechanisms, at similar but not identical locations. Pronounced differences in most frequent source directions for both wave types were reported for New Zealand by *Behr et al.* [2013], who also suggested different generation areas for the wave types. However, concerning the differences in source directions in all studies, this observation could also partly reflect the effect of the different radiation patterns, as described above.

When looking at directionally averaged wave type ratios of the strongest noise signals, we observed a temporal variation, which could be attributed to varying importance of different source areas due to seasonal variations in swell (Figure 7). The strongest seasonal ratio variations were observed at CH and GRF for southwestern directions (Figure 6a). During spring, ocean swell frequently propagated southward onto the north coast of Spain, causing a large number of high Love to Rayleigh wave ratio observations at these arrays. The generally seasonally stable azimuthal ratio pattern suggests that the proportions of the wave types are largely independent of the seasonally varying wave height levels.

A more quantitative estimation of theoretical wave type ratios would be needed to resolve the relative importance of each individual source mechanism. One must keep in mind that a simultaneous acting of several generation mechanisms and the influence of the propagation path should be taken into account.

7.2. Secondary Microseisms

For the secondary microseism band, the main findings can be summarized as follows.

1. Rayleigh waves were found to dominate the coherent noise field on average.
2. The wave type ratio shows little directional dependence.
3. The directional pattern of the wave type ratio exhibited low seasonal variations.
4. An increase in Love to Rayleigh wave ratio was found for specific source directions in central Europe.

The seismic velocity models used for kinetic energy density calculations are less well constrained at shallow depths. Therefore, the uncertainty on the exact ratio levels is higher at secondary microseism periods than for the primary microseism range. At most sites, wave type ratios generally show little azimuthal dependence, with the exception of array sites in central Europe (Figure 6b). These arrays exhibit an increase in Love to

Rayleigh wave ratio for back azimuths that coincide with directions of noise observations which often have higher phase velocities than the fundamental mode.

Dispersion curve results for the central European array THU indicate the presence of a higher Love wave mode in the noise field (see Figure 3). Resulting velocities fit well to values of the first higher mode from our local velocity structure estimation, which was retrieved from the fundamental mode dispersion curve only. Figure 3 does not necessarily show higher modes of Rayleigh waves. Moreover, an examination of dispersion curves from vertical and radial component beamformer results (not shown here) did not give a clear indication of their presence. While higher phase velocities were measured at GRF (Figure 3), they appear to be scattered and generally remained below the expected value of higher modes of either wave type.

The presence of higher mode surface waves in the microseismic noise field has been observed previously. For instance, *Kimman et al.* [2012] used an array in the Netherlands to detect fundamental and first higher mode Rayleigh waves in the secondary microseisms, with source directions pointing toward the northwest (British Isles).

Although an effort was made here to measure the ratio properties of the fundamental modes only, a possible mixture of modes or different signals with similar propagation parameters in the beamforming cannot be fully excluded here.

Despite these uncertainties, coherent Rayleigh wave observations can be measured at all the array sites. In some cases, the main Rayleigh wave directions are only weakly accompanied by coherent Love waves (Figure 5). Whenever coherent Love wave source directions were detected, they were found to generally coincide with those of Rayleigh waves (Figure 4b).

Still, in the secondary microseism band, the coherent noise field is dominated by Rayleigh waves on average. The amount of coherent Love wave measurements is clearly lower, yet considerable, with wave type energy ratios ranging from about 0.4 to 1.2 (Figure 6b) within the range of uncertainty.

The clearly lower wave type ratios in the secondary microseism range, along with the lack of directional dependence in wave type ratio, especially observed near coasts, reflect the difference in relevant source mechanisms compared to the primary microseism band. The dominance of Rayleigh waves in the coherent secondary microseismic noise field was also obtained by *Friedrich et al.* [1998] and *Nishida et al.* [2008]. Moreover, it is in agreement with the commonly accepted pressure-type source mechanism of opposing ocean waves in deep water ($2\pi h_w / \lambda_w \gg 1$), even if this mechanism does not explain any direct excitation of Love or SH waves [e.g., *Longuet-Higgins*, 1950; *Hasselmann*, 1963; *Ardhuin and Herbers*, 2013].

Since the noise field measured in central Europe has propagated across changing continental crust, an alternative explanation for the azimuthal Love to Rayleigh ratio variations could be wave type conversion along the propagation path, e.g., at the continental margin [*Gregersen and Alsop*, 1976]. The structural properties along the path can also influence the Love to Rayleigh wave ratio significantly, by altering the amplitudes of Love waves differently than those of Rayleigh waves or even inhibiting Love wave propagation [e.g., *Rind and Donn*, 1979].

Similar to the primary microseism band, the azimuthal wave type ratio pattern does not exhibit much seasonal variation (Figure 6), even for the central European arrays with azimuthal ratio variations. Since source regions are not necessarily stationary throughout the year, this would suggest that the coherent wave type ratio does not primarily depend on the location of the source but rather on permanent conditions between sources and receivers. Another possibility would be that we are unable to measure ratio variations due to source location changes since nearby source areas might dominate our results throughout the year.

8. Conclusion

We systematically compared Rayleigh and Love wave characteristics for 1 year of ocean microseisms across Europe. We found relatively stable azimuthal patterns of the Love to Rayleigh wave ratio. The directional dependence of the wave type ratio is stronger in the primary microseism band, where Love to Rayleigh wave ratios vary between 0.6 and 2.0. The strong directional dependence is likely caused by the different radiation patterns of the wave types. The high relative Love wave content hints to the presence of source mechanisms that generate strong horizontal forces.

For the secondary microseism band we find that the source directions for both wave types mainly coincide. We observe little azimuthal dependence of the wave type ratio, with the exception of central European sites, where it varies between 0.4 and 1.2. Temporal variations of the directionally averaged wave type ratio are observed and correlate with changing contributions from different source areas.

A better knowledge of the source regions and corresponding wave type ratios is desirable, in order to understand the spatial and physical origin of Love waves.

Acknowledgments
We thank Chris Bean for access to the Science Foundation Ireland (SFI) funded WaveObs array data from NW Ireland and Christine Thomas (University Münster) for access to the Morocco Münster array data. The data for all other arrays used here (GRF, IT, NICE, NOA, and THU) can be freely accessed through the GEOFON data center at http://geofon.gfz-potsdam.de. We thank the group of Fabrice Ardhuin (Ifremer, Brest) for making their modeled ocean wave parameter data available. We are grateful to Kiwamu Nishida and Toshiro Tanimoto for their useful discussions and comments. We wish to thank Oner Sufri and an anonymous reviewer for their support in improving this manuscript. This work was funded by the Emmy Noether program (HA7019/1-1) of the German Research Foundation (DFG).

References

Ardhuin, F., and T. H. Herbers (2013), Noise generation in the solid Earth, oceans and atmosphere, from nonlinear interacting surface gravity waves in finite depth, *J. Fluid Mech.*, *716*, 316–348, doi:10.1017/jfm.2012.548.

Ardhuin, F., E. Stutzmann, M. Schimmel, and A. Mangeney (2011), Ocean wave sources of seismic noise, *J. Geophys. Res.*, *116*, C09004, doi:10.1029/2011JC006952.

Ardhuin, F., L. Gualtieri, and E. Stutzmann (2015), How ocean waves rock the Earth: Two mechanisms explain microseisms with periods 3 to 300 s, *Geophys. Res. Lett.*, *42*(3), 765–772, doi:10.1002/2014GL062782.

Behr, Y., J. Townend, M. Bowen, L. Carter, R. Gorman, L. Brooks, and S. Bannister (2013), Source directionality of ambient seismic noise inferred from three-component beamforming, *J. Geophys. Res. Solid Earth*, *118*, 240–248, doi:10.1029/2012JB009382.

Beyreuther, M., R. Barsch, L. Krischer, T. Megies, Y. Behr, and J. Wassermann (2010), ObsPy: A Python toolbox for seismology, *Seismol. Res. Lett.*, *81*(3), 530–533, doi:10.1785/gssrl.81.3.530.

Brenguier, F., M. Campillo, C. Hadziioannou, N. M. Shapiro, R. M. Nadeau, and E. Larose (2008), Postseismic relaxation along the San Andreas Fault at Parkfield from continuous seismological observations, *Science*, *321*(5895), 1478–1481, doi:10.1126/science.1160943.

Brooks, L. A., J. Townend, P. Gerstoft, S. Bannister, and L. Carter (2009), Fundamental and higher-mode Rayleigh wave characteristics of ambient seismic noise in New Zealand, *Geophys. Res. Lett.*, *36*, L23303, doi:10.1029/2009GL040434.

Darbyshire, J., and H. Iyer (1958), Some recent developments in the study of microseisms in Great Britain and the United States, *Geophys. J. Int.*, *1*(2), 180–184, doi:10.1111/j.1365-246X.1958.tb00049.x.

Davy, C., G. Barruol, F. R. Fontaine, K. Sigloch, and E. Stutzmann (2014), Tracking major storms from microseismic and hydroacoustic observations on the seafloor, *Geophys. Res. Lett.*, *41*, 8825–8831, doi:10.1002/2014GL062319.

Deacon, G. (1947), Relation between sea waves and microseisms, *Nature*, *160*(4065), 419–421, doi:10.1038/160419a0.

Ebeling, C. W. (2012), Inferring ocean storm characteristics from ambient seismic noise: A historical perspective, in *Advances in Geophysics*, vol. 53, edited by R. Dmowska, pp. 1–33, Elsevier, doi:10.1016/B978-0-12-380938-4.00001-X.

Esmersoy, C., V. Cormier, and M. Toksoz (1985), Three-component array processing, in *The VELA Program. A Twenty-Five Year Review of Basic Research*, edited by A. U. Kerr, pp. 565–578, Executive Graphic Services, Arlington, Va.

Essen, H.-H., F. Krüger, T. Dahm, and I. Grevemeyer (2003), On the generation of secondary microseisms observed in northern and central Europe, *J. Geophys. Res.*, *108*(B10), 2506, doi:10.1029/2002JB002338.

Friedrich, A., F. Krüger, and K. Klinge (1998), Ocean-generated microseismic noise located with the Gräfenberg array, *J. Seismol.*, *2*(1), 47–64, doi:10.1023/A:1009788904007.

Fukao, Y., K. Nishida, and N. Kobayashi (2010), Seafloor topography, ocean infragravity waves, and background Love and Rayleigh waves, *J. Geophys. Res.*, *115*, B04302, doi:10.1029/2009JB006678.

Gerstoft, P., P. M. Shearer, N. Harmon, and J. Zhang (2008), Global P, PP, and PKP wave microseisms observed from distant storms, *Geophys. Res. Lett.*, *35*, L23306, doi:10.1029/2008GL036111.

Gregersen, S., and L. E. Alsop (1976), Mode conversion of Love waves at the continental margin, *Bull. Seismol. Soc. Am.*, *66*, 1855–1872.

Gualtieri, L., E. Stutzmann, Y. Capdeville, F. Ardhuin, M. Schimmel, A. Mangeney, and A. Morelli (2013), Modelling secondary microseismic noise by normal mode summation, *Geophys. J. Int.*, *193*(3), 1732–1745, doi:10.1093/gji/ggt090.

Gualtieri, L., E. Stutzmann, V. Farra, Y. Capdeville, M. Schimmel, F. Ardhuin, and A. Morelli (2014), Modelling the ocean site effect on seismic noise body waves, *Geophys. J. Int.*, *197*(2), 1096–1106, doi:10.1093/gji/ggu042.

Gutenberg, B. (1911), Die seismische Bodenunruhe, Doctoral thesis, Univ. of Göttingen, Germany.

Harkrider, D. G., and D. L. Anderson (1966), Surface wave energy from point sources in plane layered Earth models, *J. Geophys. Res.*, *71*(12), 2967–2980, doi:10.1029/JZ071i012p02967.

Hasselmann, K. (1963), A statistical analysis of the generation of microseisms, *Rev. Geophys.*, *1*(2), 177–210, doi:10.1029/RG001i002p00177.

Haubrich, R. A., and K. McCamy (1969), Microseisms: Coastal and pelagic sources, *Rev. Geophys.*, *7*(3), 539–571, doi:10.1029/RG007i003p00539.

Herrmann, R. B. (2013), Computer programs in seismology: An evolving tool for instruction and research, *Seismol. Res. Lett.*, *84*(6), 1081–1088, doi:10.1785/0220110096.

Iyer, H. (1958), A study on the direction of arrival of microseisms at Kew Observatory, *Geophys. J. Int.*, *1*(1), 32–43, doi:10.1111/j.1365-246X.1958.tb00032.x.

Kedar, S., M. Longuet-Higgins, F. Webb, N. Graham, R. Clayton, and C. Jones (2008), The origin of deep ocean microseisms in the North Atlantic Ocean, *Proc. R. Soc. A*, *464*, 777–793, doi:10.1098/rspa.2007.0277.

Kimman, W., X. Campman, and J. Trampert (2012), Characteristics of seismic noise: Fundamental and higher mode energy observed in the northeast of the Netherlands, *Bull. Seismol. Soc. Am.*, *102*(4), 1388–1399, doi:10.1785/0120110069.

Koper, K. D., K. Seats, and H. Benz (2010), On the composition of Earth's short-period seismic noise field, *Bull. Seismol. Soc. Am.*, *100*(2), 606–617, doi:10.1785/0120090120.

Landès, M., F. Hubans, N. M. Shapiro, A. Paul, and M. Campillo (2010), Origin of deep ocean microseisms by using teleseismic body waves, *J. Geophys. Res.*, *115*, B05302, doi:10.1029/2009JB006918.

Laske, G., G. Masters, Z. Ma, and M. Pasyanos (2013), Update on CRUST1.0—A 1-degree Global Model of Earth's Crust, *EGU General Assembly Abstract EGU2013-2658*, Vienna, Austria, 7–12 April.

Longuet-Higgins, M. S. (1950), A theory of the origin of microseisms, *Philos. Trans. R. Soc. A*, *243*(857), 1–35, doi:10.1098/rsta.1950.0012.

Matsuzawa, T., K. Obara, T. Maeda, Y. Asano, and T. Saito (2012), Love-and rayleigh-wave microseisms excited by migrating ocean swells in the North Atlantic detected in Japan and Germany, *Bull. Seismol. Soc. Am.*, *102*(4), 1864–1871, doi:10.1785/0120110269.

Nishida, K., H. Kawakatsu, Y. Fukao, and K. Obara (2008), Background Love and Rayleigh waves simultaneously generated at the Pacific Ocean floors, *Geophys. Res. Lett.*, *35*, L16307, doi:10.1029/2008GL034753.

Poggi, V., and D. Fäh (2010), Estimating Rayleigh wave particle motion from three-component array analysis of ambient vibrations, *Geophys. J. Int.*, *180*(1), 251–267, doi:10.1111/j.1365-246X.2009.04402.x.

Riahi, N., G. Bokelmann, P. Sala, and E. H. Saenger (2013), Time-lapse analysis of ambient surface wave anisotropy: A three-component array study above an underground gas storage, *J. Geophys. Res. Solid Earth*, *118*, 5339–5351, doi:10.1002/jgrb.50375.

Rind, D., and W. L. Donn (1979), Microseisms at Palisades: 2. Rayleigh wave and Love wave characteristics and the geologic control of propagation, *J. Geophys. Res.*, *84*(B10), 5632–5642, doi:10.1029/JB084iB10p05632.

Sabra, K. G., P. Gerstoft, P. Roux, W. A. Kuperman, and M. C. Fehler (2005), Surface wave tomography from microseisms in Southern California, *Geophys. Res. Lett.*, *32*, L14311, doi:10.1029/2005GL023155.

Saito, T. (2010), Love-wave excitation due to the interaction between a propagating ocean wave and the sea-bottom topography, *Geophys. J. Int.*, *182*(3), 1515–1523, doi:10.1111/j.1365-246X.2010.04695.x.

Sanchez-Sesma, F. J., and M. Campillo (2006), Retrieval of the Green's function from cross correlation: The canonical elastic problem, *Bull. Seismol. Soc. Am.*, *96*(3), 1182–1191, doi:10.1785/0120050181.

Sens-Schönfelder, C., and U. Wegler (2006), Passive image interferometry and seasonal variations of seismic velocities at Merapi Volcano, Indonesia, *Geophys. Res. Lett.*, *33*, L21302, doi:10.1029/2006GL027797.

Shapiro, N. M., and M. Campillo (2004), Emergence of broadband Rayleigh waves from correlations of the ambient seismic noise, *Geophys. Res. Lett.*, *31*, L07614, doi:10.1029/2004GL019491.

Spieker, K., I. Wölbern, C. Thomas, M. Harnafi, and L. El Moudnib (2014), Crustal and upper-mantle structure beneath the western Atlas Mountains in SW Morocco derived from receiver functions, *Geophys. J. Int.*, *198*(3), 1474–1485, doi:10.1093/gji/ggu216.

Stutzmann, E., M. Schimmel, G. Patau, and A. Maggi (2009), Global climate imprint on seismic noise, *Geochem. Geophys. Geosyst.*, *10*, Q11004, doi:10.1029/2009GC002619.

Tanimoto, T. (2013), Excitation of microseisms: Views from the normal-mode approach, *Geophys. J. Int.*, *194*, 1755–1759, doi:10.1093/gji/ggt185.

Tanimoto, T., S. Ishimaru, and C. Alvizuri (2006), Seasonality in particle motion of microseisms, *Geophys. J. Int.*, *166*(1), 253–266, doi:10.1111/j.1365-246X.2006.02931.x.

Toksöz, M. N., and R. T. Lacoss (1968), Microseisms: Mode structure and sources, *Science*, *159*(3817), 872–873, doi:10.1126/science.159.3817.872.

Tsai, V. C. (2009), On establishing the accuracy of noise tomography travel-time measurements in a realistic medium, *Geophys. J. Int.*, *178*(3), 1555–1564, doi:10.1111/j.1365-246X.2009.04239.x.

Wathelet, M. (2008), An improved neighborhood algorithm: Parameter conditions and dynamic scaling, *Geophys. Res. Lett.*, *35*, L09301, doi:10.1029/2008GL033256.

Weaver, R. L., B. Froment, and M. Campillo (2009), On the correlation of non-isotropically distributed ballistic scalar diffuse waves, *J. Acoust. Soc. Am.*, *126*(4), 1817–26, doi:10.1121/1.3203359.

Wiechert, E. (1904), Discussion, Verhandlung der zweiten Internationalen Seismologischen Konferenz, *Beitrage Zur Geophys.*, *2*, 41–43.

Zhang, J., P. Gerstoft, and P. D. Bromirski (2010), Pelagic and coastal sources of *P*-wave microseisms: Generation under tropical cyclones, *Geophys. Res. Lett.*, *37*, L15301, doi:10.1029/2010GL044288.